PLANETARY SCIENCE

The scale of a martian hydrothermal system explored using combined neutron and x-ray tomography

Josefin Martell[1]*, Carl Alwmark[1], Luke Daly[2,3,4], Stephen Hall[5,6], Sanna Alwmark[1,7,8], Robin Woracek[9], Johan Hektor[10,11], Lukas Helfen[12], Alessandro Tengattini[12,13], Martin Lee[2]

Nakhlite meteorites are igneous rocks from Mars that were aqueously altered ~630 million years ago. Hydrothermal systems on Earth are known to provide microhabitats; knowledge of the extent and duration of these systems is crucial to establish whether they could sustain life elsewhere in the Solar System. Here, we explore the three-dimensional distribution of hydrous phases within the Miller Range 03346 nakhlite meteorite using nondestructive neutron and x-ray tomography to determine whether alteration is interconnected and pervasive. The results reveal discrete clusters of hydrous phases within and surrounding olivine grains, with limited interconnectivity between clusters. This implies that the fluid was localized and originated from the melting of local subsurface ice following an impact event. Consequently, the duration of the hydrous alteration was likely short, meaning that the martian crust sampled by the nakhlites could not have provided habitable environments that could harbor any life on Mars during the Amazonian.

INTRODUCTION

Liquid water is essential to life as we know it. Consequently, the quest to understand when and where water was present on Mars has been key to understanding whether life could have existed there. In the 1970s, measurements made by the Viking lander confirmed the presence of phyllosilicates on Mars (*1*). Subsequently, hydrous minerals and related phases have been detected by several remote sensing instruments, such as the Compact Reconnaissance Imaging Spectrometer for Mars (*2*, *3*), in situ measurements and observations by Mars rovers (*4*–*6*), and in studies of martian meteorites (*7*–*12*), all of which have advanced our knowledge of the behavior of water on ancient Mars. However, until drill core samples are brought back to Earth [e.g., (*13*)], detailed laboratory analyses of martian hydrous phases are limited to those in martian meteorites [e.g., (*12*)]. Nakhlites are a group of igneous martian meteorites that are rich in pyroxene phenocrysts embedded in a fine-grained mesostasis alongside lesser amounts of olivine phenocrysts. One key finding in these meteorites is evidence for preterrestrial, martian, aqueous alteration of olivine grains (*11*, *12*). The aqueous alteration manifests in olivine grains that are, in some instances, crosscut by veins of iddingsite, which is a collective term for fine-grained hydrous minerals (e.g., smectite, iron oxy-hydroxides, and salts) that formed due to low-temperature aqueous alteration of the olivine (*11*, *14*–*16*). A martian origin of the iddingsite has been confirmed by elevated δD values in the iddingsite alteration veins (*17*) and by isotopic and chemical compositions that are consistent with in situ analyses on Mars [e.g., (*11*, *18*, *19*)].

All nakhlites found to date are thought to derive from the same volcanic system, on the basis of their similar petrology, geochemistry, and ejection age of 11 million years (Ma) (*11*, *20*). The nakhlites were emplaced in at least four magmatic events, with crystallization ages ranging from ~1416 to 1322 Ma ago (*21*). Suggested source locations are the large volcanic terrain of the Northern Plains, Tharsis, Elysium-Amazonis volcanic plains, and Syrtis Major (*22*, *23*).

The fluid alteration of the nakhlite meteorites took place on Mars ~633 ± 23 Ma ago [(*24*) and references therein] during the Amazonian period. Aqueous activity on Mars during this time is generally believed to have been limited to occasional melting of subsurface glaciers or permafrost (*25*, *26*), from which fluids could migrate within the bedrock when heated, e.g., from an impact-induced hydrothermal system (*7*, *25*, *27*). The impact event would have also served to generate a series of fractures and microstructures within the rock that allowed fluids to percolate (*7*). In the martian meteorite Miller Range (MIL) 03346, a shock deformation–driven hydrothermal system is supported by the correlation between microstructures characteristic of shock events in augite and the occurrence of secondary minerals derived from fluid-rock reactions being found within the mesostasis, connecting the shock event to the aqueous alteration (*7*). Such conditions could have provided transient habitable environments for possible martian microorganisms. However, the compositional relationships between secondary minerals and their host rock, together with the low water-to-rock ratio of the nakhlites, suggest that the solutes from which secondary minerals precipitated were sourced locally, and thus, fluids did not migrate large distances through the martian crust (*10*, *28*–*30*). Therefore, a key question regarding aqueous alteration within nakhlites and their potential as a habitable environment is: What was the extent and duration of the hydrothermal system? To accurately determine whether fluid alteration of the nakhlites was local (millimeters to centimeters) or regional (meters to kilometers), we set out to characterize the three-dimensional (3D) distribution of secondary minerals derived from water-rock reactions on Mars. To achieve this, we have combined x-ray and neutron tomography to nondestructively characterize specimens of the nakhlite MIL 03346. Furthermore, we have conducted electron backscatter diffraction analysis (EBSD) on

[1]Department of Geology, Lund University, Sölvegatan 12, 223 62 Lund, Sweden. [2]School of Geographical and Earth Sciences, University of Glasgow, Glasgow G12 8QQ, UK. [3]Australian Centre for Microscopy and Microanalysis, University of Sydney, Sydney 2006, NSW, Australia. [4]Department of Materials, University of Oxford, Oxford OX1 3PH, UK. [5]Division of Solid Mechanics, Lund University, Lund, Sweden. [6]Lund Institute of Advanced Neutron and X-ray Science (LINXS), Lund, Sweden. [7]Niels Bohr Institute, University of Copenhagen, Copenhagen, Denmark. [8]Natural History Museum Denmark, University of Copenhagen, Copenhagen, Denmark. [9]European Spallation Source, Lund, Sweden. [10]LUNARC, Centre for Scientific and Technical Computing, Lund University, Lund, Sweden. [11]Department of Materials Science and Applied Mathematics, Malmö University, Malmö, Sweden. [12]Institut Laue-Langevin, Grenoble, France. [13]Universite Grenoble Alpes, CNRS, Grenoble INP, 3SR, Grenoble, France.
*Corresponding author. Email: josefin.martell@geol.lu.se

a polished slab of the sample to investigate the relationship between altered phases and shock deformation and scanning electron microscopy (SEM)–EBSD imaging to verify the tomography results.

X-ray and neutron imaging

Neutron tomography is a nondestructive 3D imaging method that has shown promising results in the field of earth sciences (*31*) and is frequently used in paleontology but has also been used in a few, relatively recent, studies of planetary materials (*32*–*36*), including structural characterization of iron meteorites (*32*). Neutron interaction with matter differs from that of x-rays, as it does not follow a linear relationship with atomic number. Accordingly, the same minerals will have different attenuation coefficients for the two modalities where, e.g., hydrogen and boron will yield high neutron attenuation, while minerals rich in elements such as iron are comparatively lower attenuating to neutrons than to x-rays (*37*, *38*). X-ray computed tomography (XCT) is a conventional method for nondestructive 3D imaging (*39*–*43*) and an excellent technique to detect and image minerals comprising heavy elements; neutron tomography has a complementary contrast, essential in delineating, for example, hydrous phases from anhydrous phases of similar x-ray attenuation, and thus enables pinpointing of hydrous material. In studies where hydrous phases are of particular interest, combining neutrons and x-rays provides a powerful tool for nondestructive analysis of mineral textures, modal mineral abundances, and shape orientations of a whole suite of minerals (*37*, *44*, *45*).

RESULTS

Hydrous phases in olivine and mesostasis

The reflected light optical photomicrograph of the interior of the MIL 03346,230 sample (Fig. 1A) exposes two contrasting regions: a yellow-tinted region that is crosscut by several large fractures and a less deformed region where both relatively euhedral, dark-green augite grains and mesostasis can be easily distinguished. Reflected light and backscatter electron (BSE) imaging reveal that the mesostasis in the less deformed regions contains skeletal titanomagnetite and, in a few instances, titanomagnetite with twinning. In contrast, the yellow-tinted region (outlined in Fig. 1, A and B) is characterized by heavily fractured augite grains and one heavily altered olivine grain containing pervasive iddingsite veins (Fig. 1, C and D). In the upper right part of the sample is one slightly larger, ~0.6-mm olivine grain. Both olivine grains are more easily discerned in the BSE image (Fig. 1, B, C, and E) and are both crosscut by <10-μm veins of iddingsite (Fig. 1, C and E), where the veins' orientations appear to be crystallographically controlled with a weak preferred orientation [similar to, e.g., (*10*)]. The iddingsite is also distinguished by a dark red color in reflected light photomicrographs (Fig. 1, D and F). The upper right olivine grain (Fig. 1, E and F) contains a network of fractures but appears slightly less affected by aqueous alteration than the other olivine grain. This observation is confirmed by the neutron images (Fig. 2), where hydrous components occur more abundantly in the upper left part of the sample. For a detailed description of other phases in MIL 03346, consistent with the observations in our study, the reader is referred to (*9*, *15*–*17*, *46*, *47*).

3D renderings of olivine and hydrous constituents

Thresholding of the tomography data enables separation between different mineral phases. Figure 2 (A to D) shows 3D renderings of MIL 03346,230 where olivine grains and hydrous constituents have been highlighted. Tomography reveals that, aside from the two olivine grains exposed in the BSE images, the sample also contains two slightly smaller olivine grains. Three of the olivine grains are somewhat

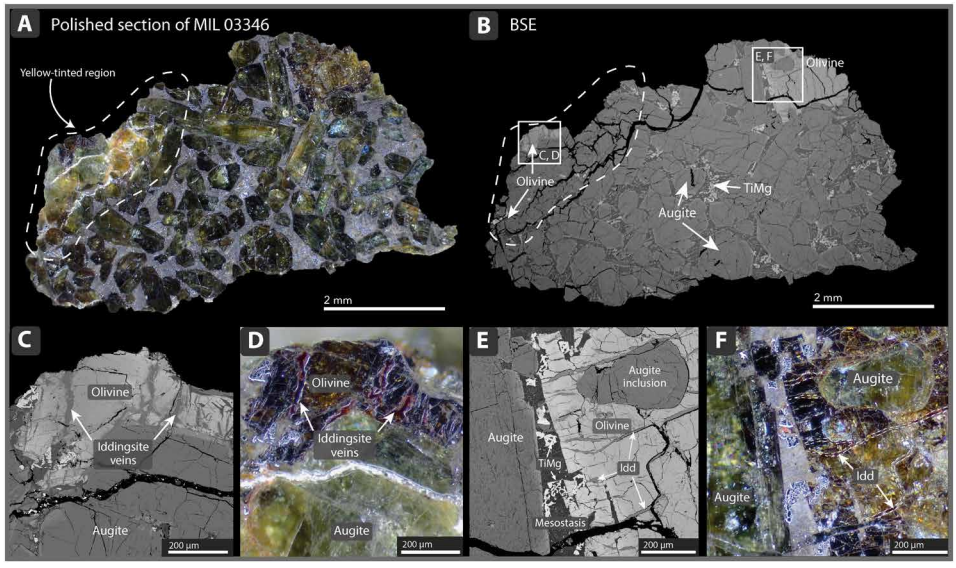

Fig. 1. A polished section of MIL 03346,230. (**A**) Photograph of the interior of MIL 03346,230. Note the yellow tint in the left region of the sample, marked by dotted lines. Mineral grains in the yellow-tinted region are heavily affected by aqueous alteration. (**B**) BSE image of the same section as in (A). Light gray olivine grains, marked with arrows, are situated in the altered areas. The white boxes show locations for detailed images in (C) to (F). (**C**) BSE image of the upper left olivine grain, marked with a box in (B). Iddingsite veins are cutting through a fractured olivine grain. Augite grains and a fine-grained mesostasis (dark gray) containing titanomagnetite (bright, skeletal grains) are also shown in the figure. (**D**) Photograph of the upper left olivine grain, same as in (C). Iddingsite veins have a dark red color. (**E**) BSE image showing details of the upper right olivine grain. The grain is fractured and crosscut by iddingsite veins that are predominantly oriented east to west in the image. (**F**) Photograph of the same grain as in (E), where the dark red iddingsite veins have been outlined.

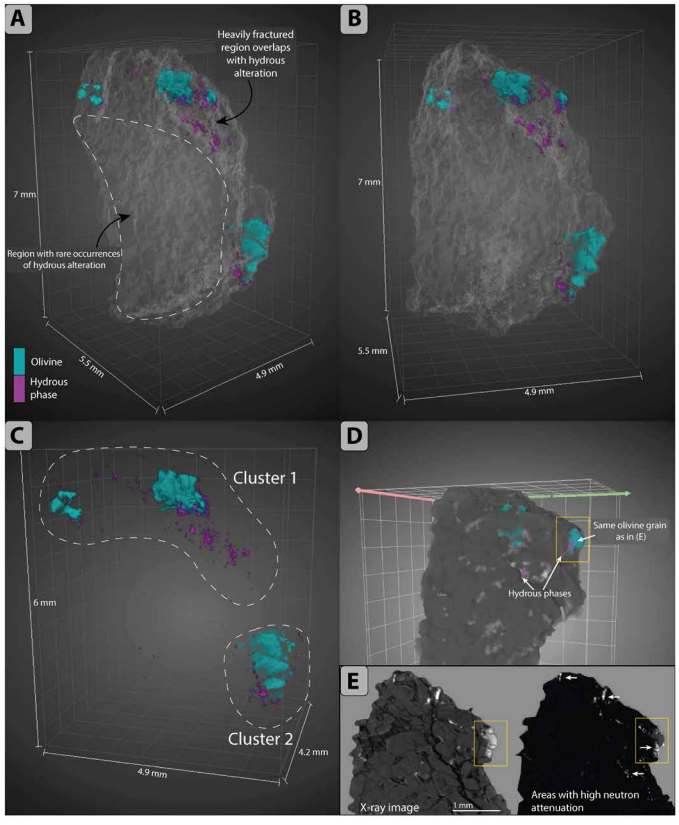

Fig. 2. Combined x-ray and neutron volumes of MIL 03346,230. (**A** and **B**) 3D renderings of the sample, where olivine (based on x-ray volume) and hydrous constituents (based on neutron volume) have been segmented and combined. Other phases are transparent; however, the outline of the sample has been kept for context. Voxel size is 7.15 μm. (**C**) Same 3D rendering as in (A) and (B) but without the sample outline to better discern individual features. Two clusters have been outlined, on the basis of their relationship to the hydrous material. Cluster 1 corresponds to the highly altered and fractured area in Figs. 1 (A to D) and 3. The olivine grain in cluster 2 appears less altered than cluster 1, and there is a limited connectivity between the two clusters. The scarce, magenta-colored points that have not been outlined correspond to mesostasis. (**D**) The sample was clipped to show part of the interior. The gray background is from the x-ray volume, where the bright mineral corresponds to titanomagnetite; this mineral occurs within the whole sample. Part of the large fracture that is visible in the altered area of Fig. 1, and its relationship to the hydrous material, can also be seen in this image. The yellow box marks one olivine grain that is also visible in (E). (**E**) X-ray image and a corresponding slice where areas of high neutron attenuation have been highlighted (also shown with arrows). The yellow boxes correspond to the olivine grain marked in (D).

clustered together (Fig. 2). The hydrous phases appear to center around the olivine grains and extend from these via fractures in the mesostasis. There is no visible interconnectivity of hydrous phases between clusters 1 and 2 (Fig. 2). The correlation between hydrous constituents and olivine grains and, to some extent, the association between hydrous material and the fractured area (yellow-tinted in Fig. 1) can be seen when comparing single corresponding slices from the neutron and x-ray volumes. Figure 2E depicts one such slice—first, by showing only the high-resolution x-ray image where the major mineral phases are easily discerned, and second, by showing the same x-ray image at reduced resolution, overlain with highly attenuating phases from the corresponding neutron tomography slice (see also figs. S1 and S2). The hydrous phases are visible as bright features in and around the right-side olivine grain and in parts of the mesostasis. Minor, local regions of hydrous constituents outside the clusters can also be found distributed within the mesostasis of the meteorite (Fig. 2A). A 3D rendering of MIL 03346,231 that shows similar clustering of hydrous phases can be found in the Supplementary Materials (fig. S3). Video renderings of both samples are also available in the same file (movies S1 and S2).

EBSD map of shock textures

Crystallographic orientation EBSD data were collected from a ~2-mm^2 region of the polished section of MIL 03346,230 (Fig. 3A), selected because of the high abundance of aqueous alteration phases (see also Fig. 1A). The band contrast image (Fig. 3B) visualizes the quality of the electron backscatter diffraction patterns (EBSPs); the quality can be a result of the degree of crystallinity where higher crystallinity (brighter areas) yields better EBSPs (and, thus, a higher-quality mapping), differential polishing, and beam sensitivity of the phases. Figure 3C shows the grain-relative orientation distribution (GROD) angle map, which represents internal misorientation relative to the average orientation of the grain. The GROD angle map color bar ranges from blue to red, where green-yellow-red colors represent an increased degree of internal misorientation (maximum GROD angle was 10°) relative to the grain average. Within the analyzed area, internal deformation increases toward the yellow-tinted region, where grains are more fractured, and individual grains can display an internal misorientation of up to 10°. Figure 3D shows an EBSD map with an inverse pole figure (IPF) coloring scheme, where different colors correspond to different grain orientations. Several augite phenocrysts show mechanical twinning [attributed to shock, e.g., (*48*)] and simple twinning (marked with arrows in Fig. 3D). The occurrence of mechanical twins is also correlated with areas of high internal misorientations, consistent with (*7*).

DISCUSSION

The tomography results from both MIL 03346 specimens (Fig. 2 and fig. S3) show a relationship between olivine grains and hydrous phases, which is consistent with previous studies of MIL 03346 [(*9*) and references therein], as well as with SEM imaging from this study, showing that iddingsite veins crosscut both of the olivine grains in the polished section (Fig. 1). Since neutrons are sensitive to hydrogen, the hydrous-phase iddingsite is expected to be easily visible as high-attenuation volumes in the neutron data, although individual iddingsite veins were difficult to resolve because of limitations in spatial resolution (voxel width of 7.15 μm). Nevertheless, the neutron data show that clusters of high-attenuating phases are located in, or in the vicinity of, the olivine grains in the sample. The distribution of the hydrous phases can be determined when the dataset is rendered in 3D (Fig. 2 and fig. S3); the hydrogen content is greater in the yellow-tinted part of the sample, which is consistent with the SEM images where the olivine grain in this region exhibits more intense aqueous alteration compared to the olivine grain in Fig. 1 (E and F). The EBSD results of MIL 03346,230 show that aqueous alteration assemblages correspond to areas of elevated shock deformation microstructures in augite, as previously reported in (*7*). The shock deformation and localized peak shock temperatures likely facilitated the melting of ice and ingress of water, thus enabling aqueous alteration of olivine and mesostasis (*7*). In terms of interconnectivity between hydrous clusters, the 3D data presented here

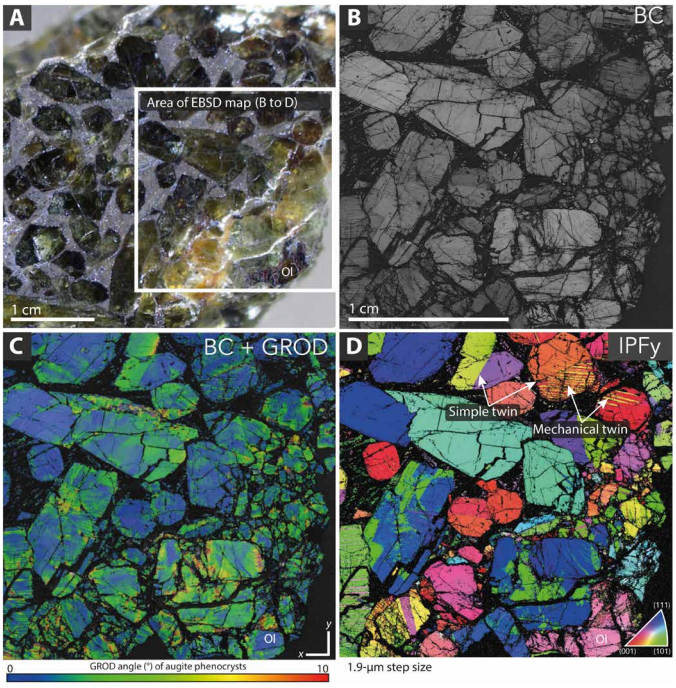

Fig. 3. Part of the polished section, chosen for EBSD analysis. (**A**) Photograph of part of the polished section; note the difference between more pristine, dark green augite grains in a grayish mesostasis on the left-hand side of the image and more deformed augite grains, situated in a fractured, yellow-tinted region. The white box outlines where EBSD orientation data (B to D) were collected. (**B**) Band contrast image, showing the relative quality of EBSPs. Lower-quality EBSP (progressively darker regions) correlates with regions of heavy fracturing. (**C**) GROD angle EBSD map showing internal deformation of augite grains. The color scale represents increasing deformation from green to red, while undeformed regions are blue. (**D**) IPF map (IPFy) where different colors represent different orientations. Examples of simple twins and mechanical twins in augite are marked with arrows and occur in the whole map. Ol, olivine. Same scale in (C) and (D) as in (B).

uniquely reveal that fluid alteration within this sample was local to the olivine but that shock-induced fractures enabled fluids to extend into portions of the mesostasis in the vicinity of the olivine grains. The minor and highly localized (neutron) high-attenuating material within the mesostasis (Fig. 2, A to C) could not be correlated with shock in this study, but altered mesostasis in isolated, olivine-free regions has previously been correlated with heavily shocked regions in other specimens of the MIL 03346 meteorite (*7*). The same study also reported the occurrence of unaltered mesostasis in several highly shocked regions. Together, this implies that the fluid source was not external, thus ruling out a large-scale percolation of fluids from the martian surface through this rock. Instead, the most probable source of water would be local subsurface ices within the rock that melted during a pulse of high temperature following an impact event [e.g., (*7*, *49*)]. This interpretation is consistent with (*29*), which determined low water/rock ratios for iddingsite formation in the nakhlite Lafayette, suggesting that their formation did not take place during extensive water flushing and instead occurred briefly at low temperatures. The correlation of the chemical composition of iddingsite and its host rock (*28*) furthermore rules out precipitation of a fluid that had migrated from another rock unit.

To assess the possibility of a (microbial) habitable environment in the source rocks of the nakhlites, the duration of liquid water in the rocks (hydrothermal system) and the temperature are crucial factors. In a study of phyllosilicates in several nakhlites (*49*), it was concluded that the source of aqueous alteration was a hydrothermal system, with a duration on the order of a month. This is in agreement with previous studies also suggesting a short duration system with temperatures <100°C as the source of aqueous alteration in the Lafayette meteorite (*29*, *30*). The limited extent and minimal to no interconnectivity of 3D aqueous alteration assemblages observed by neutron tomography support a short duration period of fluid activity that was derived from local fluids and a low water-rock ratio. This suggests that the impact event that provided the energy to melt subsurface ices was relatively small, or the nakhlite source region was toward the periphery of the impact structure. In addition, we infer that in the nakhlite source region, habitable conditions were short-lived (days to months) and localized to volumes of millimeter scale and were therefore unlikely to provide stable havens for microorganisms on Mars during the Amazonian period.

Combined neutron tomography and XCT for future sample return missions

The combined use of neutron tomography and XCT has an outstanding potential for nondestructive analysis of samples and requires little or no sample preparation. Therefore, these techniques are ideal for conducting first assessment 3D investigations of the precious samples to be returned from Mars by the Mars Sample Return mission campaign [e.g., (*13*)]. While conventional XCT by itself can be used to distinguish between many common minerals, it cannot be used to identify and outline hydrous constituents in minerals, i.e., of similar x-ray attenuation. X-ray phase-contrast imaging is sensitive to the electron density, and in consequence, it needs many hydrogen atoms (in comparison to more heavy elements) to substantially modify the electron density. The neutron interacts strongly with hydrogen atoms, and as a result, neutron tomography is very sensitive to the presence of hydrogen and can thus reveal the 3D distribution of hydrous phases. Besides contributing valuable insights into water-rock interactions in extraterrestrial material, the data can be used to make informed decisions on what samples/sections to choose for further analysis, possibly saving pristine material for future research; thus, the complementarity use of these two imaging techniques should be considered for future Mars sample return missions.

To conclude, our correlative neutron/XCT-SEM investigations of the martian nakhlite meteorite MIL 03346 reveal that aqueous alteration assemblages are localized into discrete volumes and are likely not part of a larger, interconnected fracture network. This implies that the fluid source did not derive from a larger-scale hydrothermal system. The lack of interconnectivity in 3D implies that martian hydrous alteration was localized within the meteorite, involved only small volumes of fluid, and was likely short-lived. Fluids were most likely derived from small amounts of subsurface ices found within the rock itself. The correlation between shock microstructures and aqueous alteration assemblages indicates that the heat source for melting this ice was an impact event, consistent with previous interpretations. Impact cratering processes and their associated hydrothermal systems are thought to provide transient, potentially habitable environments that could act as safe havens for life. Thus, our results have direct implications for the habitability of the martian subsurface in the nakhlite source region, where any habitable environments were localized and very short-lived, reducing the chance of life's emergence or survival on Mars during the Amazonian period.

MATERIALS AND METHODS

Sample description

MIL 03346 is paired with three other finds: MIL 090030, MIL 090032, and MIL 090136. Interstitial to the augite and olivine phenocrysts in MIL 03346 is a fine-grained mesostasis consisting of minerals including skeletal titanomagnetite, pyrrhotite, and apatite (*7*, *11*, *15*, *50*). The augite grains have average core compositions of $W^{38–42}En^{35–40}Fs^{22–28}$ and narrow hedenbergite rims where augite grain boundaries are in contact with the mesostasis. Occurrences of iddingsite in olivine and mesostasis have previously been correlated with areas of shock deformation (*7*). This study considers two MIL 03346 nakhlite specimens (acquired from NASA): (i) MIL 03346,230 (the studied sample is approximately 0.7 cm by 0.7 cm by 0.7 cm in size and weighs 0.250 g) and (ii) MIL 03346,231 (the studied sample is approximately 0.4 cm by 0.4 cm by 0.3 cm in size and weighs 0.290 g) (see fig. S3).

Tomography and registration of volumes

Neutron tomography data were acquired at the NeXT instrument at Institut Laue-Langevin in Grenoble, France (*51*). The samples were placed in a cylindrical Teflon sample holder, and 1792 neutron radiographic projections, each the result of 3 individual projections lasting 9.5 s, were acquired over a 180° rotation, using a source pinhole size of 15 mm and a distance from the pinhole to the sample of 10 m (giving a collimation, "L/D," ratio of 667). Given a sample/detector distance of about 4 to 5 mm, this should give a neutron penumbra (blurring) below 10 μm, which corresponds to the thickness of the scintillator. This value should be considered as a rough estimate of the true spatial resolution. The neutron flux under these conditions was 9×10^7 n s^{-1} cm^{-2}, and the mean neutron energy for the instrument is 12.3 meV (corresponding to a neutron wavelength of 3 Å). Tomographic reconstruction was performed using filtered back projection with the XAct reconstruction software from RXSolutions to yield tomographic image volumes with cubic voxels of dimension 7.15 μm. The selected voxel size was a compromise between spatial resolution and measurement time. While XCT data were also acquired at the NeXT beamline with the same setup and without removing the samples, higher-resolution XCT images, acquired with a Zeiss Xradia XRM520 at the 4D imaging laboratory at Lund University, were used for the combined x-ray and neutron analysis. These data were acquired with 1601 projections over 360° with a source voltage of 60 kV and a power of 5 W with the manufacturer-supplied Le5 source filter. For the MIL 03346,231 sample, the reconstructed cubic voxel width was 5.75 μm, and for the MIL 03346,230 sample, it was 9 μm.

A nonrigid transformation to align the neutron tomography and XCT volumes was made using the SPAM software (*52*). From the spatially registered images, it was possible to derive a dual histogram (fig. S2) that plots reconstructed attenuation coefficients of the two datasets. In both samples, the aim was to map out hydrous phases, which are easily discerned with neutrons, and correlate these to the correct mineral phases, which are better resolved with x-rays (e.g., Fe- and Mg-rich minerals such as augite and olivine). Individual slices were visualized in Fiji (*53*), and segmentation and volume renderings were generated using Dragonfly software version 2021.1 Build 977 (*54*). Olivine grains were manually segmented from the x-ray volume to avoid the inclusion of phases with overlapping gray scales, and hydrous constituents were segmented from the neutron volume by thresholding the neutron histogram. After segmentation of the highly attenuating hydrous phase in the neutron tomography, the neutron volume image was dilated (kernel of 3 × 3) to connect spatially coherent grayscale values and then eroded twice (kernel of 3 × 3) to remove isolated single voxels. Using both modalities, a final, combined volume was produced, showing both the nominally anhydrous mineralogy and how it relates to hydrous phases (iddingsite) in three dimensions. Furthermore, the nondestructive nature of the method guaranteed that the sample was not contaminated during the data collection. Video renderings of both samples were generated using Dragonfly; these are provided in the Supplementary Materials (movies S1 and S2).

Scanning electron microscopy–electron backscatter diffraction analysis

To verify the validity of the segmentation of the tomography data into different phases, as well as to collect orientation data of shock textures in individual mineral grains, the analyzed sample of MIL 03346,230 was cast in epoxy and polished to expose an interior surface. For scanning electron microscopy (SEM) imaging, the sample was coated with ~15 nm of carbon. The images were acquired with a Tescan Mira3 High-Resolution Schottky field-emission SEM, equipped with an Oxford Energy-Dispersive X-ray Spectroscopy system (X-MaxN 80, 124 eV, 80 mm^2), an EBSD high-resolution detector (Symmetry S2, Oxford Instruments), and a cathodoluminescence system, located at the Department of Geology, Lund University, Sweden, operating at 20 kV/2 nA and in high vacuum. To ease the process of aligning corresponding neutron tomography, XCT, and SEM images, additional XCT images were made of the epoxy-embedded sample, both before and after cutting/polishing.

Following SEM imaging, carbon coating was removed with ethanol, and EBSPs were collected from a selected section of the same polished surface to reveal internal misorientations and shock textures in the grains. Before the EBSD measurements, the sample was polished until smooth with colloidal silica suspended in a NaOH solution, coated with a <5-nm carbon layer to avoid charging, and attached to a 70° pretilted specimen holder. Orientation data were collected with a high-resolution EBSD detector, operating in low vacuum at an acceleration voltage of 15 kV and a beam current of 10 nA. EBSPs were collected using a band detection minimum/maximum of 6/8, high gain, and a step size of 1.9 μm, at a working distance of ~14 mm. Match units used were augite (*55*) and olivine (*56*). Pole figures and orientation maps were constructed using Aztec Crystal. The EBSD data were processed to remove noise by applying a wild-spike noise reduction to remove isolated pixels, followed by a six-point iterative nearest neighbor correction to improve twin and grain boundaries without creating substantial artifacts standard for EBSD (*57*). The pole figures were plotted using an equal-area, upper hemisphere projection and an IPF coloring scheme to reveal internal misorientation and grain boundaries in the sample. Grain boundaries were defined as a >10° misorientation between adjacent pixels. Mechanical twins in augite were defined by a 180° rotation around the ⟨100⟩ axis, forming twin planes parallel to (001), and simple mirror twins in augite were defined by a 180° rotation around ⟨001⟩ with twin planes parallel to (100).

SUPPLEMENTARY MATERIALS

Supplementary material for this article is available at https://science.org/doi/10.1126/sciadv.abn3044

REFERENCES AND NOTES

1. P. Toulmin III, A. K. Baird, B. C. Clark, K. Keil, H. J. Rose Jr., R. P. Christian, P. H. Evans, W. C. Kelliher, Geochemical and mineralogical interpretation of the Viking inorganic chemical results. *J. Geophys. Res.* **82**, 4625–4634 (1977).
2. J. Carter, F. Poulet, J. P. Bibring, N. Mangold, S. Murchie, Hydrous minerals on Mars as seen by the CRISM and OMEGA imaging spectrometers: Updated global view. *J. Geophys. Res. Planets* **118**, 831–858 (2013).
3. C. I. Fassett, J. W. Head, D. T. Blewett, C. R. Chapman, J. L. Dickson, S. L. Murchie, S. C. Solomon, T. R. Watters, Caloris impact basin: Exterior geomorphology, stratigraphy, morphometry, radial sculpture, and smooth plains deposits. *Earth Planet. Sci. Lett.* **285**, 297–308 (2009).
4. G. Klingelhöfer, R. V. Morris, B. Bernhardt, C. Schröder, D. S. Rodionov, P. A. de Souza, A. Yen, R. Gellert, E. N. Evlanov, B. Zubkov, J. Foh, U. Bonnes, E. Kankeleit, P. Gütlich, D. W. Ming, F. Renz, T. Wdowiak, S. W. Squyres, R. E. Arvidson, Jarosite and hematite at Meridiani Planum from Opportunity's Mössbauer spectrometer. *Science* **306**, 1740–1745 (2004).
5. W. Rapin, B. Chauviré, T. S. J. Gabriel, A. C. McAdam, B. L. Ehlmann, C. Hardgrove, P. Y. Meslin, B. Rondeau, E. Dehouck, H. B. Franz, N. Mangold, S. J. Chipera, R. C. Wiens, J. Frydenvang, S. Schröder, In situ analysis of opal in Gale Crater, Mars. *J. Geophys. Res. Planets* **123**, 1955–1972 (2018).
6. S. W. Squyres, J. P. Grotzinger, R. E. Arvidson, J. F. Bell III, W. Calvin, P. R. Christensen, B. C. Clark, J. A. Crisp, W. H. Farrand, K. E. Herkenhoff, J. R. Johnson, G. Klingelhöfer, A. H. Knoll, S. M. McLennan, H. Y. McSween Jr., R. V. Morris, J. W. Rice Jr., R. Rieder, L. A. Soderblom, In situ evidence for an ancient aqueous environment at Meridiani Planum, Mars. *Science* **306**, 1709–1714 (2004).
7. L. Daly, M. R. Lee, S. Piazolo, S. Griffin, M. Bazargan, F. Campanale, P. Chung, B. E. Cohen, A. E. Pickersgill, L. J. Hallis, P. W. Trimby, R. Baumgartner, L. V. Forman, G. K. Benedix, Boom boom pow: Shock-facilitated aqueous alteration and evidence for two shock events in the martian nakhlite meteorites. *Sci. Adv.* **5**, eaaw5549 (2019).
8. P. Gillet, J. A. Barrat, E. Deloule, M. Wadhwa, A. Jambon, V. Sautter, B. Devouard, D. Neuville, K. Benzerara, M. Lesourd, Aqueous alteration in the Northwest Africa 817 (NWA 817) martian meteorite. *Earth Planet. Sci. Lett.* **203**, 431–444 (2002).
9. L. J. Hallis, G. J. Taylor, Comparisons of the four Miller Range nakhlites, MIL 03346, 090030, 090032 and 090136: Textural and compositional observations of primary and secondary mineral assemblages. *Meteorit. Planet. Sci.* **46**, 1787–1803 (2011).
10. M. R. Lee, T. Tomkinson, L. J. Hallis, D. F. Mark, Formation of iddingsite veins in the martian crust by centripetal replacement of olivine: Evidence from the nakhlite meteorite Lafayette. *Geochim. Cosmochim. Acta* **154**, 49–65 (2015).
11. A. H. Treiman, The nakhlite meteorites: Augite-rich igneous rocks from Mars. *Geochemistry* **65**, 203–270 (2005).
12. A. Udry, G. H. Howarth, C. D. K. Herd, J. M. D. Day, T. J. Lapen, J. Filiberto, What Martian meteorites reveal about the interior and surface of Mars. *J. Geophys. Res. Planets* **125**, e2020JE006523 (2020).
13. K. A. Farley, K. H. Williford, K. M. Stack, R. Bhartia, A. Chen, M. de la Torre, K. Hand, Y. Goreva, C. D. K. Herd, R. Hueso, Y. Liu, J. N. Maki, G. Martinez, R. C. Moeller, A. Nelessen, C. E. Newman, D. Nunes, A. Ponce, N. Spanovich, P. A. Willis, L. W. Beegle, J. F. Bell III, A. J. Brown, S.-E. Hamran, J. A. Hurowitz, S. Maurice, D. A. Paige, J. A. Rodriguez-Manfredi, M. Schulte, R. C. Wiens, Mars 2020 mission overview. *Space Sci. Rev.* **216**, 142 (2020).
14. T. E. Bunch, A. M. Reid, The nakhlites part I: Petrography and mineral chemistry. *Meteoritics* **10**, 303–315 (1975).
15. M. D. Dyar, A. H. Treiman, C. M. Pieters, T. Hiroi, M. D. Lane, V. O'Connor, MIL03346, the most oxidized Martian meteorite: A first look at spectroscopy, petrography, and mineral chemistry. *J. Geophys. Res. Planets* **110**, E09005 (2005).
16. M. Anand, C. Williams, S. Russell, G. Jones, S. James, M. Grady, Petrology and geochemistry of nakhlite MIL 03346: A new Martian meteorite from Antarctica, paper presented at the 36th Lunar and Planetary Science Conference, Houston, Texas, USA, 14 to 18 March 2005.
17. L. J. Hallis, G. J. Taylor, K. Nagashima, G. R. Huss, A. W. Needham, M. M. Grady, I. A. Franchi, Hydrogen isotope analyses of alteration phases in the nakhlite martian meteorites. *Geochim. Cosmochim. Acta* **97**, 105–119 (2012).
18. A. Udry, J. M. D. Day, 1.34 Billion-year-old magmatism on Mars evaluated from the co-genetic nakhlite and chassignite meteorites. *Geochim. Cosmochim. Acta* **238**, 292–315 (2018).
19. C. M. Corrigan, M. A. Velbel, E. P. Vicenzi, Modal abundances of pyroxene, olivine, and mesostasis in nakhlites; heterogeneity, variation, and implications for nakhlite emplacement. *Meteorit. Planet. Sci.* **50**, 1497–1511 (2015).
20. L. E. Nyquist, D. D. Bogard, C. Y. Shih, A. Greshake, D. Stöffler, O. Eugster, Ages and geologic histories of Martian meteorites. *Space Sci. Rev.* **96**, 105–164 (2001).
21. B. E. Cohen, D. F. Mark, W. S. Cassata, M. R. Lee, T. Tomkinson, C. L. Smith, Taking the pulse of Mars via dating of a plume-fed volcano. *Nat. Commun.* **8**, 640 (2017).
22. J. C. Bridges, S. P. Schwenzer, The nakhlite hydrothermal brine on Mars. *Earth Planet. Sci. Lett.* **359-360**, 117–123 (2012).
23. J. C. Bridges, P. H. Warren, The SNC meteorites: Basaltic igneous processes on Mars. *J. Geol. Soc. London* **163**, 229–251 (2006).
24. L. Borg, M. J. Drake, A review of meteorite evidence for the timing of magmatism and of surface or near-surface liquid water on Mars. *J. Geophys. Res. Planets* **110**, E12S03 (2005).
25. H. G. Changela, J. C. Bridges, Alteration assemblages in the nakhlites: Variation with depth on Mars. *Meteorit. Planet. Sci.* **45**, 1847–1867 (2010).
26. K. E. Scanlon, J. W. Head, D. R. Marchant, Volcanism-induced, local wet-based glacial conditions recorded in the Late Amazonian Arsia Mons tropical mountain glacier deposits. *Icarus* **250**, 18–31 (2015).
27. G. R. Osinski, L. L. Tornabene, N. R. Banerjee, C. S. Cockell, R. Flemming, M. R. M. Izawa, J. McCutcheon, J. Parnell, L. J. Preston, A. E. Pickersgill, A. Pontefract, H. M. Sapers, G. Southam, Impact-generated hydrothermal systems on Earth and Mars. *Icarus* **224**, 347–363 (2013).
28. M. R. Lee, L. Daly, B. E. Cohen, L. J. Hallis, S. Griffin, P. Trimby, A. Boyce, D. F. Mark, Aqueous alteration of the Martian meteorite Northwest Africa 817: Probing fluid–rock interaction at the nakhlite launch site. *Meteorit. Planet. Sci.* **53**, 2395–2412 (2018).
29. A. H. Treiman, R. A. Barrett, J. L. Gooding, Preterrestrial aqueous alteration of the Lafayette (SNC) meteorite. *Meteoritics* **28**, 86–97 (1993).
30. A. H. Treiman, D. Lindstrom, Trace element geochemistry of martian iddingsite in the Lafayette meteorite. *J. Geophys. Res.* **102**, 9153–9163 (1997).
31. A. Tengattini, N. Lenoir, E. Andò, G. Viggiani, Neutron imaging for geomechanics: A review. *Geomech. Energy Environ.* **27**, 100206 (2021).
32. S. Caporali, F. Grazzi, F. Salvemini, U. Garbe, S. Peetermans, G. Pratesi, Structural characterization of iron meteorites through neutron tomography. *Minerals* **6**, 14 (2016).
33. A. Fedrigo, K. Marstal, C. Bender Koch, V. Andersen Dahl, A. Bjorholm Dahl, M. Lyksborg, C. Gundlach, F. Ott, M. Strobl, Investigation of a Monturaqui impactite by means of bi-modal X-ray and neutron tomography. *J. Imaging* **4**, 72 (2018).
34. S. E. Kichanov, D. P. Kozlenko, E. V. Lukin, A. V. Rutkauskas, E. A. Krasavin, A. Y. Rozanov, B. N. Savenko, A neutron tomography study of the Seymchan pallasite. *Meteorit. Planet. Sci.* **53**, 2155–2164 (2018).
35. S. Steen Duchnik, M. Lanzky, L. Steffensen Schmidt, "X-ray and neutron tomography of the Allende meteorite," thesis, Copenhagen University, Copenhagen (2012).
36. A. H. Treiman, J. M. LaManna, L. M. Anovitz, D. S. Hussey, D. L. Jacobson, Neutron computed tomography of meteorites: Detecting hydrogen-bearing materials, paper presented at the 49th Lunar and Planetary Science Conference, 1 March 2018.
37. G. D. Gatta, K. Hradil, M. Meven, Where is the hydrogen? *Elements* **17**, 163–168 (2021).
38. N. Kardjilov, I. Manke, R. Woracek, A. Hilger, J. Banhart, Advances in neutron imaging. *Mater. Today* **21**, 652–672 (2018).
39. J. M. Friedrich, M. L. Rivers, Three-dimensional imaging of ordinary chondrite microporosity at 2.6 μm resolution. *Geochim. Cosmochim. Acta* **116**, 63–70 (2013).
40. D. C. Hezel, J. M. Friedrich, M. Uesugi, Looking inside: 3D structures of meteorites. *Geochim. Cosmochim. Acta* **116**, 1–4 (2013).
41. T. Matsumoto, A. Tsuchiyama, K. Nakamura-Messenger, T. Nakano, K. Uesugi, A. Takeuchi, M. E. Zolensky, Three-dimensional observation and morphological analysis of organic nanoglobules in a carbonaceous chondrite using X-ray micro-tomography. *Geochim. Cosmochim. Acta* **116**, 84–95 (2013).
42. R. D. Hanna, R. A. Ketcham, X-ray computed tomography of planetary materials: A primer and review of recent studies. *Geochemistry* **77**, 547–572 (2017).
43. A. W. Needham, R. L. Abel, T. Tomkinson, M. M. Grady, Martian subsurface fluid pathways and 3D mineralogy of the Nakhla meteorite. *Geochim. Cosmochim. Acta* **116**, 96–110 (2013).
44. G. Artioli, D. S. Hussey, Imaging with neutrons. *Elements* **17**, 189–194 (2021).
45. R. D. Hanna, R. A. Ketcham, Evidence for accretion of fine-grained rims in a turbulent nebula for CM Murchison. *Earth Planet. Sci. Lett.* **481**, 201–211 (2018).
46. A. Udry, H. Y. McSween Jr., P. Lecumberri-Sanchez, R. J. Bodnar, Paired nakhlites MIL 090030, 090032, 090136, and 03346: Insights into the Miller Range parent meteorite. *Meteorit. Planet. Sci.* **47**, 1575–1589 (2012).
47. N. Imae, Y. Ikeda, Petrology of the Miller Range 03346 nakhlite in comparison with the Yamato-000593 nakhlite. *Meteorit. Planet. Sci.* **42**, 171–184 (2007).
48. D. Stöffler, K. Keil, E. R. D. Scott, Shock metamorphism of ordinary chondrites. *Geochim. Cosmochim. Acta* **55**, 3845–3867 (1991).
49. J. C. Bridges, D. C. Catling, J. M. Saxton, T. D. Swindle, I. C. Lyon, M. M. Grady, Alteration assemblages in Martian meteorites: Implications for near-surface processes. *Space Sci. Rev.* **96**, 365–392 (2001).
50. F. M. McCubbin, N. J. Tosca, A. Smirnov, H. Nekvasil, A. Steele, M. Fries, D. H. Lindsley, Hydrothermal jarosite and hematite in a pyroxene-hosted melt inclusion in martian meteorite Miller Range (MIL) 03346: Implications for magmatic-hydrothermal fluids on Mars. *Geochim. Cosmochim. Acta* **73**, 4907–4917 (2009).

51. A. Tengattini, N. Lenoir, E. Andò, B. Giroud, D. Atkins, J. Beaucour, G. Viggiani, NeXT-Grenoble, the neutron and X-ray tomograph in Grenoble. *Nucl. Instrum. Method Phys. Res. A* **968**, 163939 (2020).
52. O. Stamati, E. Andò, E. Roubin, R. Cailletaud, M. Wiebicke, G. Pinzon, C. Couture, R. C. Hurley, R. Caulk, D. Caillerie, T. Matsushima, P. Bésuelle, F. Bertoni, T. Arnaud, A. O. Laborin, R. Rorato, Y. Sun, A. Tengattini, O. Okubadejo, J.-B. Colliat, M. Saadatfar, F. E. Garcia, C. Papazoglou, I. Vego, S. Brisard, J. Dijkstra, G. Birmpilis, spam: Software for practical analysis of materials. *J. Open Source Softw.* **5**, 2286 (2020).
53. J. Schindelin, I. Arganda-Carreras, E. Frise, V. Kaynig, M. Longair, T. Pietzsch, S. Preibisch, C. Rueden, S. Saalfeld, B. Schmid, J.-Y. Tinevez, D. J. White, V. Hartenstein, K. Eliceiri, P. Tomancak, A. Cardona, Fiji: An open-source platform for biological-image analysis. *Nat. Methods* **9**, 676–682 (2012).
54. Dragonfly 2021.1 [Computer software]. Object Research Systems (ORS) Inc, Montreal, Canada, 2021; software available at http://www.theobjects.com/dragonfly.
55. A. Gualtieri, Accuracy of XRPD QPA using the combined Rietveld–RIR method. *J. Appl. Cryst.* **33**, 267–278 (2000).
56. M. Haiber, P. Ballone, M. Parrinello, Structure and dynamics of protonated Mg_2SiO_4: An ab-initio molecular dynamics study. *Am. Mineral.* **82**, 913–922 (1997).
57. M. Bestmann, D. J. Prior, Intragranular dynamic recrystallization in naturally deformed calcite marble: Diffusion accommodated grain boundary sliding as a result of subgrain rotation recrystallization. *J. Struct. Geol.* **25**, 1597–1613 (2003).

Acknowledgments: We acknowledge N. Tsapatsaris, who initially loaned the samples from NASA; E. Andó and E. Törnquist, who both helped with the SPAM software; and N. Kardjilov for helpful discussions on data analysis. We are also grateful for the support in the image analysis provided by the Quantification of Imaging Data from MAX IV (QIM) project at Lund University and the QuantIm hackathon at LINXS (Lund Institute of Advanced Neutron and X-ray Science) and to the Extraterrestrial Materials Analysis Group (ExMAG) at NASA that allocated the samples. Two anonymous reviewers, as well as R. Klima, are thanked for helpful comments and suggestions that improved this work. **Funding:** This work was supported by the Royal Physiographic Society of Lund grant 40957 (to J.M.), the Swedish Research Council grant 2017-06388 (to S.A.), and the Swedish Research Council grant 621-2012-4504 (to C.A.). The data were acquired at Institut Laue-Langevin, https://doi.ill.fr/10.5291/ILL-DATA.UGA-79. **Author contributions:** Conceptualization: L.D., C.A., S.H., J.M., S.A., and R.W. Collection of neutron/x-ray tomograms: S.H., L.H., and A.T. SEM-EBSD: J.M., C.A., and L.D. Registration of tomograms: J.M. and J.H. Segmentation and rendering: J.M. Supervision: R.W., C.A., and L.D. Writing—original draft: J.M., L.D., C.A., and S.A. Writing—review and editing: All authors. **Competing interests:** The authors declare that they have no competing interests. **Data and materials availability:** The meteorite specimens MIL 03346,230 and MIL 03346,231 are loaned from the Extraterrestrial Materials Analysis Group (ExMAG) at NASA and are currently held at Lund University, Sweden. U.S. Antarctic meteorite samples are recovered by the Antarctic Search for Meteorites (ANSMET) program, which has been funded by NSF and NASA, and characterized by the Department of Mineral Sciences of the Smithsonian Institution and Astromaterials Acquisition and Curation Office at the NASA Johnson Space Center. The raw data are available at zenodo.org under the DOI: 10.5281/zenodo.6365242 (https://zenodo.org/record/6365242#.Yj3HIurMKUI).

Submitted 20 December 2021
Accepted 28 March 2022
Published 11 May 2022
10.1126/sciadv.abn3044